The Astrophysical Journal, 1000:94 (11pp), 2026 March 20 https://doi.org/10.3847/1538-4357/ae48e6

On the Origin of Coronal Picoflare Jets

Annu Bura[1,2], Daniel Nóbrega-Siverio[3,4,5,6], Tanmoy Samanta[1,2], and Jayant Joshi[1]
[1] Indian Institute of Astrophysics, Koramangala, Bangalore 560034, India; tanmoy.samanta@iiap.res.in
[2] Pondicherry University, R.V. Nagar, Kalapet 605014, Puducherry, India
[3] Instituto de Astrofísica de Canarias, E-38205 La Laguna, Tenerife, Spain
[4] Universidad de La Laguna, Dept. Astrofísica, E-38206 La Laguna, Tenerife, Spain
[5] Rosseland Centre for Solar Physics, University of Oslo, PO Box 1029 Blindern, 0315 Oslo, Norway
[6] Institute of Theoretical Astrophysics, University of Oslo, PO Box 1029 Blindern, 0315 Oslo, Norway
Received 2025 November 5; revised 2026 January 22; accepted 2026 February 19; published 2026 March 16

Abstract

Small-scale jet-like eruptions, such as picoflare jets and jetlets, are recognized as potential contributors to coronal heating and solar wind acceleration, yet their physical origin is still not fully established. Using ultra-high-resolution extreme ultraviolet imaging datasets from the Extreme Ultraviolet Imager on board the Solar Orbiter mission, we investigate tiny coronal jets observed off-limb in the Sun's polar regions. Visual inspection reveals that the majority of these jets exhibit distinct morphological features, including a bright spire accompanied by a dark, eruptive jet component. We analyzed 11 of these jets in detail and found that their spatial and temporal scales are comparable to previously reported jetlets, while their kinetic energies are two to three orders of magnitude lower, placing them in the picoflare regime. The bright and dark components show distinct dynamics, with the dark structures generally displaying lower speeds. A comparison with coordinated Interface Region Imaging Spectrograph data and the Atmospheric Imaging Assembly on board the Solar Dynamics Observatory data, together with 2.5D radiative-MHD simulations performed with the Bifrost code, reveals a one-to-one morphological correspondence between the dark counterparts and cool chromospheric surges accompanying the bright jet spire. This association suggests that flux emergence and magnetic reconnection at low atmospheric heights may produce coupled bright–dark structures, providing a plausible mechanism for the generation of picoflare jets. Our results demonstrate Solar Orbiter's ability to resolve the dynamics of small-scale jets and place new constraints on their origin.

Unified Astronomy Thesaurus concepts: Solar corona (1483); Solar coronal heating (1989); Polar jets (1274); Solar magnetic reconnection (1504); Solar spicules (1525); Solar chromosphere (1479); Solar transition region (1532)

Materials only available in the online version of record: animations

1. Introduction

Solar coronal jets are collimated plasma ejections from the solar atmosphere and are observed across a wide range of wavelengths (for a review of jets, see N. E. Raouafi et al. 2016; Y. Shen 2021; B. Schmieder 2022), from X-rays (K. Shibata et al. 1992; R. C. Canfield et al. 1996; M. Shimojo et al. 1996; R. L. Moore et al. 2010; A. C. Sterling et al. 2015, 2022) to Extreme Ultraviolet (EUV; D. E. Innes et al. 1997; F. Moreno-Insertis et al. 2008; G. Nisticò et al. 2009; J. S. He et al. 2010; H. Tian et al. 2014; A. C. Sterling & R. L. Moore 2016; R. Joshi et al. 2020; D. Nóbrega-Siverio et al. 2025), and sometimes exhibit both cool and hot plasma components.

Beyond the large-scale coronal jets, the solar atmosphere hosts numerous jet-like phenomena in the transition region and chromosphere at even smaller spatial and temporal scales, such as transition-region network jets (H. Tian et al. 2014; N. Narang et al. 2016; H. Tian et al. 2018; J. Gorman et al. 2022), chromospheric jets (D. Kuridze et al. 2011; X. Bai et al. 2019; R. Joshi et al. 2024; A. Bhatnagar et al. 2025; A. Bura et al. 2025a), and spicules (B. de Pontieu et al. 2007; T. M. D. Pereira et al. 2012, 2014; T. Samanta et al. 2015, 2019; S. Bose et al. 2021, 2023). These small-scale eruptions, which are more frequent and shorter-lived than coronal jets, provide a potential mechanism for supplying plasma and energy to the outer corona and solar wind (T. Samanta et al. 2019; Y. Shen 2021; L. P. Chitta et al. 2023; N. E. Raouafi et al. 2023; S. Bose et al. 2025).

In coronal jets, we often observed the cool component as a surge or filament eruption in Hα or EUV images, whereas the hot component observed as bright EUV or X-ray spires (J. Chae et al. 1999; R. L. Moore et al. 2013; H. Chen et al. 2009; S. M. Mulay et al. 2017; Y. Shen et al. 2017; A. C. Sterling et al. 2020). Surges, for instance, are chromospheric ejections that reach coronal heights and are commonly observed in Hα and other chromospheric lines as dark, elongated structures (J. R. Roy 1973; B. Schmieder et al. 1984; Y. C. Jiang et al. 2007; W. Uddin et al. 2012; H. Tian et al. 2018; D. Nóbrega-Siverio et al. 2024). They are most often associated with emerging flux regions and are frequently accompanied by hot EUV or X-ray jets, indicating that magnetic reconnection between newly emerging and ambient fields is a primary driver (K. Shibata et al. 1992; T. Yokoyama & K. Shibata 1996; S. Vargas Domínguez et al. 2014; F. Moreno-Insertis & K. Galsgaard 2013; D. Nóbrega-Siverio et al. 2016). Filament eruptions, particularly at small scales (often termed "minifilament eruptions"; A. C. Sterling et al. 2015), are usually linked to flux cancellation events and have been observed in EUV images from the Atmospheric Imaging Assembly (AIA; J. R. Lemen et al. 2012) on board Solar Dynamics Observatory (SDO; W. D. Pesnell et al. 2012) as absorption features, especially in the He II 304 Å channel. The

destabilization and eruption of these minifilaments drive the jet spire, while magnetic reconnection beneath the erupting structure produces the associated Jet Bright Point (JBP; J. Hong et al. 2011; Y. Shen et al. 2012; M. Adams et al. 2014; A. C. Sterling et al. 2015, 2016; P. F. Wyper et al. 2017; P. Kumar et al. 2019; A. C. Sterling & R. L. Moore 2020). These observations of coexisting bright and dark components in coronal jets motivate the investigation of similar features at smaller spatial and temporal scales, where tiny jet-like eruptions may provide crucial insight into the physical processes driving these multithermal structures.

Many numerical simulations have also investigated the ejection of hot (bright spire) and cool (dark surge) plasma associated with magnetic flux emergence through the low atmosphere into the corona (T. Yokoyama & K. Shibata 1996; R. L. Jiang et al. 2012; F. Moreno-Insertis & K. Galsgaard 2013; D. Nóbrega-Siverio et al. 2016; L. Yang et al. 2018; X. Li et al. 2023). While such models reproduce surge-like ejections successfully, realistic radiative-MHD simulations of minifilament eruptions are still lacking. Therefore, to directly validate these processes, we require observations capable of resolving the intricate dynamics of both bright and dark plasma structures in jet evolution.

The Extreme Ultraviolet Imager (EUI; P. Rochus et al. 2020) on board Solar Orbiter (D. Müller et al. 2020) provides such capability, offering unprecedented spatial resolution and high cadence. With these advances, EUI has revealed numerous small-scale transient events, such as campfires (D. Berghmans et al. 2021; N. K. Panesar et al. 2021; F. Kahil et al. 2022; N. Narang et al. 2025), tiny inverted Y-shaped coronal jets with energies in the nanoflare and picoflare ranges (S. Mandal et al. 2022; N. K. Panesar et al. 2023; L. P. Chitta et al. 2023, 2025; F. Shi et al. 2024), and nanojets (A. Bura et al. 2025b; Y. Gao et al. 2025). These studies highlight the potential role of small-scale jet-like eruptions, such as jetlets (N. E. Raouafi et al. 2023; A. C. Sterling et al. 2024) and picoflare jets (L. P. Chitta et al. 2023, 2025), in contributing significantly to the mass and energy flux of the solar wind. Among these, picoflare jets represent the smallest resolved reconnection-driven jets observed to date and they have been suggested as potential contributors to coronal heating and solar wind acceleration. They have widths of $\sim$100 km, evolve on timescales of 20–100 s, and often show inverted Y-shaped structures. Yet, their physical origin remains elusive.

In this study, we combine high-resolution EUI observations with numerical simulations to investigate tiny coronal jets observed off-limb in the Sun's polar regions. By leveraging our unique observations, which reveal both bright and dark components at very small spatial scales, we aim to shed light on the origin of picoflare jets.

2. Data Analysis, Results, and Discussion

2.1. Observations and Data Reduction

We investigate the bright and dark structures of tiny coronal jets observed off-limb in the Sun's polar regions. While such coupled bright and dark structures are commonly observed in larger coronal jets, in our work we investigate similar features at smaller spatial and temporal scales using High Resolution Imager (HRI) data on board Solar Orbiter with the aim of gaining insight into their underlying physical processes. For this purpose, we reviewed the publicly available $\mathrm{HRI_{EUV}}$ animation datasets from Solar Orbiter, focusing on off-limb observations. Through the visual inspection of these observations we noticed that the majority of jets display the simultaneous presence of a bright spire and a narrow, collimated dark structure. From these, we selected 10 well-isolated jets from four datasets in which the bright and dark structures could be clearly distinguished and whose evolution could be followed. In total, we analyzed 11 coronal jets using these four $\mathrm{HRI_{EUV}}$ datasets, along with one coordinated observation from the Interface Region Imaging Spectrograph (IRIS; B. De Pontieu et al. 2014) and AIA on board SDO. Our analysis is focused on the $\mathrm{HRI_{EUV}}$ channel centered at 174 Å, which is mainly sensitive to plasma at temperatures of $\sim$1.0 MK.

Table 1 provides a comprehensive summary of the observations analyzed in this study. During the first dataset (hereafter D1), acquired on 2021 September 14, Solar Orbiter was located at a heliocentric distance of $\sim$0.587 au. $\mathrm{HRI_{EUV}}$ observed the north solar pole from 03:19 UT to 04:18 UT with a cadence of 20 s and a pixel scale of $0\farcs492$, corresponding to a pixel size of $\sim$0.210 Mm. The second observation (hereafter D2), also on 2021 September 14, covered the south polar region from 04:35 UT to 05:50 UT at a cadence of 20 s, and from 05:53 UT to 06:11 UT at a higher cadence of 5 s, with the same pixel scale of $\sim$0.210 Mm. The third observation (hereafter D3), conducted on 2022 March 30 when Solar Orbiter was at $\sim$0.332 au, observed the south pole from 04:30 UT to 04:59 UT. This dataset provided enhanced temporal and spatial resolution with a cadence of 3 s and a pixel size of $\sim$0.120 Mm. The fourth observation at the west limb (hereafter D4), taken on 2024 April 5 at a heliocentric distance of $\sim$0.295 au, covered the time interval from 19:59 UT to 23:34 UT with a cadence of 16 s and a pixel size of $\sim$0.105 Mm. We analyzed one jet from D1, two jets from D2, six jets from D3, and one jet from D4.

The full width at half-maximum (FWHM) of the core of the point-spread function of $\mathrm{HRI_{EUV}}$ is about two pixels (D. Berghmans et al. 2021; L. P. Chitta et al. 2023), corresponding to a spatial resolution of $0\farcs984$, which is $\sim$0.420 Mm for D1 and D2, $\sim$0.240 Mm for D3, and $\sim$0.210 Mm for D4. We used level 2 datasets of $\mathrm{HRI_{EUV}}$ from the latest EUI data release 6.0 (E. Kraaikamp et al. 2023). To mitigate the effects of residual spacecraft jitter in the data, we followed the approach described in L. P. Chitta et al. (2022), which was also employed in earlier $\mathrm{HRI_{EUV}}$ observations (A. Bura et al. 2025b).

With the aim of providing a complementary analysis, in the fifth dataset (hereafter D5), we analyzed coordinated observations from IRIS and AIA, acquired on 2019 August 7. For this observation, IRIS performed a 64-step raster scan covering a field of view (FOV) of $22'' \times 119''$. The step size and raster cadence were 1.2 s and 74 s, respectively. The observation, targeting a coronal hole at the north pole, was conducted from 22:00 UT to 23:00 UT, with IRIS pointing centered at $(-0\farcs715, 828\farcs867)$. The plate scale was $0\farcs3327$ pixel^{-1}. IRIS provided slit-jaw images (SJIs) in the 2832 Å passband at a cadence of 9 s, which is mainly sensitive to the plasma emission from the upper photosphere at a temperature of $T \sim 10^{3.8}$ K. We used level 2 data for our analysis. For the AIA data we used the 171 Å passband, which is sensitive to emission from Fe IX, with a characteristic formation temperature of $T \sim 10^{5.8}$ K. We calibrated AIA data using the `aia_prep.pro` routine available in SolarSoft. To co-align

Table 1
Summary of the Observations Analyzed in this Study

Dataset	Date	Time (UT)	Instrument	Location	Distance (au)	Cadence	Pixel Scale (arcsec)	Resolved Kilometers on the Sun	No. of Jets Analyzed
D1	2021-09-14	03:19–04:18	HRI_{EUV}	North pole	0.587	20 s	0.492	420	1 (Jet 1)
D2	2021-09-14	04:35–05:50	HRI_{EUV}	South pole	0.587	20 s	0.492	420	2 (Jet 2, Jet 3)
		05:53–06:11				5 s			
D3	2022-03-30	04:30–04:59	HRI_{EUV}	South pole	0.332	3 s	0.492	240	6 (Jet 4—Jet 9)
D4	2024-04-05	19:59–23:34	HRI_{EUV}	West limb	0.295	16 s	0.492	210	1 (Jet 10)
D5	2019-08-07	22:00–23:00	IRIS	North pole	1.0	74 s (Raster)	0.33	480	1 (Jet 11)
			AIA			12 s	0.6	870	

the IRIS and AIA data, we matched photospheric features in images from both IRIS SJI 2832 Å and the AIA 1700 Å passband.

2.2. Numerical Experiment

To provide support to our observations we use a radiative-MHD numerical simulation performed with the Bifrost code (B. V. Gudiksen et al. 2011). The experiment, presented and described in detail in D. Nóbrega-Siverio et al. (2017, 2018), is a 2.5D simulation of magnetic flux emergence in a coronal hole that leads to the formation of a coronal jet along with a surge. The realism of the simulation has proven to be valuable for understanding the transition-region emission of surges observed with IRIS. In addition, it has been used to explain plasmoid signatures in chromospheric and transition-region lines (L. Rouppe van der Voort et al. 2017). As shown in the following section, it also shares resemblance with the observed jets and dark structures presented in this study.

2.3. Dynamical Properties of Bright and Dark Structures

Figure 1 shows jets observed at the solar poles using HRI_{EUV} on board Solar Orbiter in the 174 Å passband. Each jet exhibits a bright spire and a collimated dark structure (indicated by white arrows) and has the shape of an inverted "Y" (or "λ") shape (K. Shibata et al. 1994; T. Yokoyama & K. Shibata 1995). These bright and dark structures are the primary focus of the analysis presented in this study.

We analyzed the morphological and dynamical properties of both the bright jet spires and their associated dark structures. To estimate the width of these structures, we placed an artificial slit (shown as a white solid line in panels (a) and (c) of Figure 2) across the jet, intersecting both the bright and dark structures. We employed the same method for all of the jets, and for illustrative purposes, we have shown only cases 1 and 6. To maintain a uniform orientation across all jets and facilitate visual interpretation we mirrored the images of jet 1 about the y-axis, bringing the structure of the jet in line with the typical jet morphology commonly seen in the literature associated with jets (K. Shibata et al. 1992; R. C. Canfield et al. 1996). The corresponding intensity profiles along these slit are shown as histograms in panels (b) and (d). To quantify the width, we fitted two separate Gaussian functions: one to the intensity peak representing the bright jet spire (red curve), and the other to the intensity dip corresponding to the dark structure (blue curve). The FWHM of these Gaussian fits provides a measure of their width. This analysis was applied consistently across all jets in the dataset. We found that the width of the bright spire ranges from 0.35 to 1.75 Mm with a mean value of 0.69 Mm, while the width of the dark structure ranges from 0.23 to 0.83 Mm with a mean value of 0.49 Mm. We also estimated the projected length of these jets from the jet base at the visible surface to the top of the spire using a cubic spline interpolation method. For this analysis we visually selected four points along the jet axis and interpolated them to 100 points using the IDL routine spline.pro to obtain a smooth curve. We repeated this procedure five times to reduce bias from manual selection and took the average as the final jet length. The resulting spline-interpolated curve is shown as a green dashed curve in panels (a) and (c) for jet 1 and jet 6, respectively. From this analysis, we found that the jet lengths range from approximately 7.85–29.74 Mm, with a mean length of 16.90 Mm. We estimated the uncertainties in the measured jet lengths from repeated spline measurements and found them to be very small relative to the jet lengths. For example, for jet 1 shown in panel (a) of Figure 2 the uncertainty was ~0.12 Mm.

To estimate the propagation speeds of both the bright jet spires and the associated dark structures we constructed spacetime diagrams by placing two separate artificial slits along the direction of jet propagation, one along the bright jet spire (indicated by a white dashed rectangular box) and the other along the dark structure (yellow dashed rectangular box), as shown in panels (a) and (d) of Figure 3 for jets 4 and 5. Within these slits, the maximum intensity values were extracted for the bright spire (white slit) at each timestamp, while the minimum intensity values were extracted for the dark structure (yellow slit) to construct their respective spacetime diagrams. The corresponding spacetime diagrams for the bright spires are displayed in panels (b) and (e), while those for the dark structures are shown in panels (c) and (f) of Figure 3. In the spacetime diagrams, the motion of the upper parts of both structures appears as inclined ridges. By manually tracking these ridges and measuring their slopes, we estimated their projected plane-of-sky speeds. From this spacetime analysis, we find that the bright jet spires have speeds ranging from 43 to 132 km s^{-1} (mean: 85 km s^{-1}), while the dark structures propagate more slowly, with speeds between 30 and 67 km s^{-1} (mean: 49 km s^{-1}). These measured jet speeds represent the motion of the upper part of the bright spire rather than the bulk plasma flow, as the latter is often difficult to track due to mixed flows. However, we find that the uncertainties in the measured speeds, estimated from five repeated measurements of the ridge positions, are very small and therefore unlikely to significantly affect the derived kinetic energy of the bright spire. For example, in the case of jet 4, shown in panel (a) of Figure 3, the uncertainties were 2.7 and 1.3 km s^{-1} for the bright and dark structures, respectively. We note, however, that these uncertainty values should be considered as lower limits, as projection effects also complicate the estimation of the speed and its associated uncertainties. These estimated speed values are consistent with previously reported speeds for chromospheric ejections, such as surges, based on both observations (B. Schmieder et al. 1984; J. Chae et al. 1999; H. Yang et al. 2013; M. Verma et al. 2020; D. Nóbrega-Siverio et al. 2024) and numerical simulations (F. Moreno-Insertis & K. Galsgaard 2013; D. MacTaggart et al. 2015; D. Nóbrega-Siverio et al. 2016; X. Li et al. 2023). In all cases, the bright jet spire moves faster than the associated dark structures. The lifetimes of the jets were determined by visually tracking the duration over which they remained discernible in the time series. Their lifetime ranges from 3.4 to 11.5 minutes, with an average lifetime of approximately 6.2 minutes. The measured properties of the observed jets are summarized in Table 2.

We find that the spatial and temporal scales of our jets lie between those of picoflare jets and jetlets. L. P. Chitta et al. (2023) reported that picoflare jets are a few hundred kilometers wide, have speeds of the order of 100 km s^{-1}, and carry kinetic energies in the picoflare range. Our events show bright spire widths of 0.35–1.75 Mm, lengths of 7.85–29.74 Mm, lifetimes of 3.4–11.5 minutes, and spire speeds of 43–132 km s^{-1}. These size and lifetime values are also consistent with reported jetlet properties (widths: 0.6–3 Mm, lengths: 9–27 Mm, and

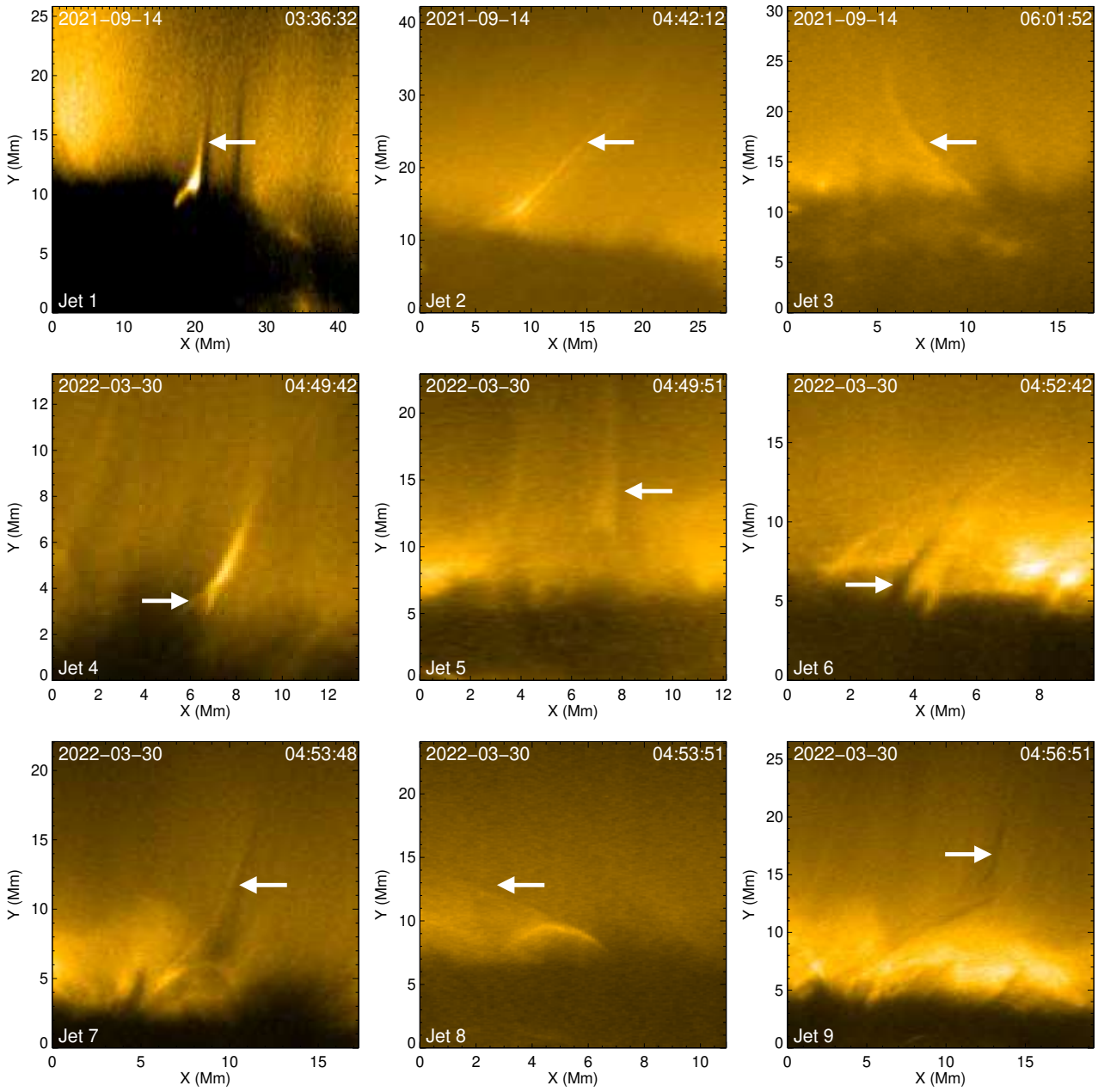

Figure 1. Examples of jets observed off-limb in the Sun's polar regions using HRI_{EUV} on board Solar Orbiter with a passband centered at 174 Å, each accompanied by a narrow, collimated dark structure indicated by the white arrows. These jets are selected from three datasets: the north pole observation on 2021 September 14 (jet 1), the south pole observations on 2021 September 14 (jets 2–3), and on 2022 March 30 (jets 4–9). An animation of this figure is available online. The animation start/end times are given in each panel of the animation for each jet. The real-time duration of the animation is 10 s.

(An animation of this figure is available in the online article.)

lifetimes up to several minutes; N. K. Panesar et al. 2019; N. E. Raouafi et al. 2023), while the propagation speeds are comparable to picoflare jets. However, L. P. Chitta et al. (2023) did not report any associated dark structures in their study. One reason could be that most of their jets were observed on-disk where strong background emission makes it difficult to detect faint absorption features. By contrast, our jets are observed off-limb at the Sun's polar regions where the reduced background brightness allows dark structures to be seen more clearly. Another possibility is that their jets are smaller in spatial and temporal scales compared to ours, which makes it harder to identify any associated dark counterparts. Moreover, we require enough dense and cool material to absorb the EUV emission from the background, which is primarily due to the presence of neutral hydrogen and helium (He I and He II; U. Anzer & P. Heinzel 2005), otherwise dark structures may remain too transparent to be observed.

The properties of our jets are also comparable to the thin jets associated with coronal bright points, as reported in a recent study by D. Nóbrega-Siverio et al. (2025). However, no dark structures were detected in those coronal bright point–related jets, likely due to differences in the driving mechanisms. Furthermore, in comparison to spicules, which have widths of 0.2–0.5 Mm, lengths of 5–10 Mm, a lifetime of 5–15 minutes, and rise with speeds of 15–150 km s^{-1} (B. de Pontieu et al. 2007; T. M. D. Pereira et al. 2012; T. Samanta et al. 2015), our

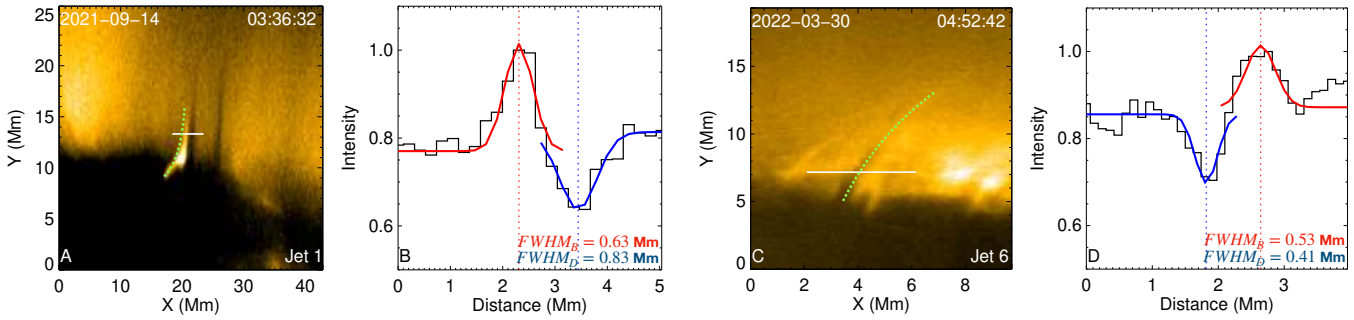

Figure 2. Width estimation for jets observed in HRI_{EUV}. Panel (a) shows the observation of jet 1 in HRI_{EUV} with a white artificial slit marking the location used to extract the intensity profile. Panel (b) shows the corresponding intensity profile (histogram mode) where two Gaussian functions are fitted to the peak (red curve) and dip (blue curve) in the profile, corresponding to the adjacent bright and dark structures, to estimate their FWHM. Panels (c) and (d) show a similar analysis for jet 6. The green dashed curve in panels (a) and (c) represents the spline-interpolated curve from the jet base at the visible surface to the top of the spire, used to estimate the jet lengths.

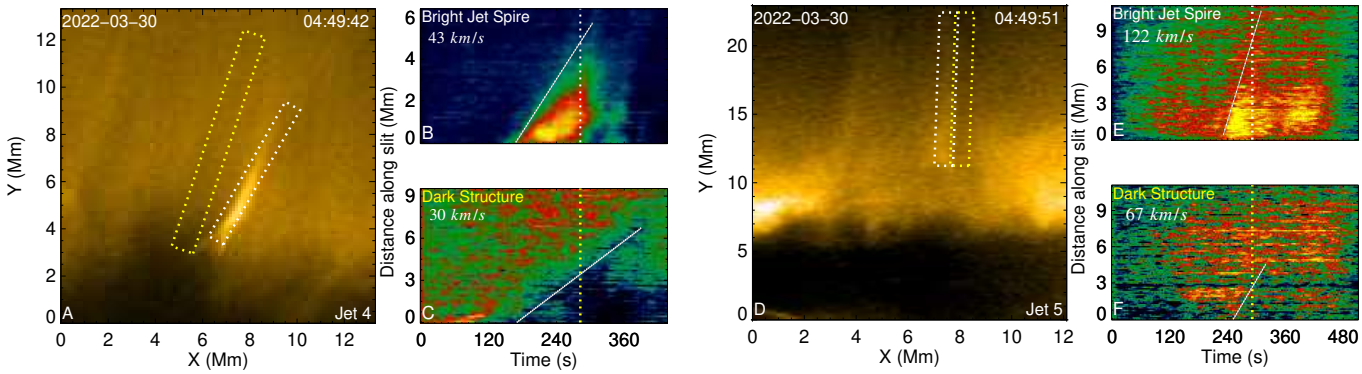

Figure 3. Speed estimations of jets observed in HRI_{EUV}. Panel (a) shows jet 4 in HRI_{EUV} with two artificial slits overlaid: a white rectangle (5 pixels wide) and a yellow rectangle (7 pixels wide), used to construct spacetime diagrams for the bright jet spire and the associated dark structure, respectively. Panels (b) and (c) display the resulting spacetime plots along these artificial slits. For the bright jet spire, the maximum intensity values along the white slit are used to construct the spacetime diagram, and the propagation speed is obtained by tracking the inclined intensity ridge corresponding to the upper part of the spire. For the dark structure, the minimum intensity values along the yellow slit are used in an analogous manner. Panels (d)–(f) present the same analysis for jet 5.

Table 2
Measured Properties of the Observed Jets in HRI_{EUV} on Board Solar Orbiter

Jet No.	Bright Spire Width (Mm)	Dark Structure Width (Mm)	Bright Spire Speed (km s^{-1})	Dark Structure Speed (km s^{-1})	Length (Mm)	Lifetime (minutes)	Bright Spire Kinetic Energy (erg)
1	0.63	0.83	65	55	8.67	5.00	1.91×10^{22}
2	1.75	⋯	⋯	⋯	29.74	7.00	⋯
3	0.89	0.77	63	⋯	24.18	3.40	9.98×10^{22}
4	0.63	0.67	43	30	7.58	5.35	7.30×10^{21}
5	0.47	0.23	122	67	21.09	4.55	9.10×10^{22}
6	0.53	0.41	63	39	13.05	4.90	1.91×10^{22}
7	0.37	0.45	106	65	15.65	10.15	3.16×10^{22}
8	0.63	0.28	63	⋯	13.31	4.45	2.75×10^{22}
9	⋯	⋯	132	47	23.74	5.70	⋯
10	0.35	0.28	110	39	12.03	11.46	2.34×10^{22}

Note. The ellipses indicate where properties could not be measured reliably.

jets occupy a comparatively larger spatio-temporal scale. Interestingly, T. Samanta et al. (2019) reported that enhanced spicular activity can channel hot plasma into the corona and heat the upper solar atmosphere. In their on-disk observations, spicules manifest as dark features in Hα, with coronal emission in AIA 171 Å generally appearing at their tops. An open question that arises is whether spicules share the same underlying origin as the coupled bright–dark structures revealed in our EUI jets. We expect that future high-resolution, multiwavelength observations will provide the critical evidence needed to establish or refute this connection.

2.4. Kinetic Energy of Jets

We further estimated jet kinetic energies for the bright spire using the standard relation $E_k = \frac{1}{2} n_e m_p v^2 V$, with the jet volume approximated as $V = \frac{\pi L w^2}{4}$, where L and w are the measured jet length and width, respectively. Assuming a coronal-hole electron density of $n_e = 2 \times 10^8\,\mathrm{cm}^{-3}$ (U. Feldman et al. 1978; L. P. Chitta et al. 2023), the resulting kinetic energies lie between 7.30×10^{21} erg and 9.98×10^{22} erg (mean: 3.98×10^{22} erg). These values place our jets above the lower limit reported for picoflare jets

($\gtrsim 10^{21}$ erg; L. P. Chitta et al. 2023) but below the total energies quoted for jetlets (10^{24}–10^{25} erg; N. E. Raouafi et al. 2023; A. C. Sterling et al. 2024). Energetically, our jets are therefore consistent with the picoflare energy regime, while their spatial sizes and lifetimes are consistent with jetlets. We note that these kinetic energy estimates depend on the assumed density, volume, projection, and length estimation and are therefore subject to uncertainties.

2.5. Comparison with the Flux-emergence Simulation

We further examined the temporal evolution of jets and compared them with the flux-emergence simulation of D. Nóbrega-Siverio et al. (2017, 2018), introduced in Section 2.2. Figure 4 presents three representative observational cases (jets 10, 1, and 7) in panels (a)–(c), followed by the synthetic emission in the EUI 174 Å filter of the simulation (panel (d)), temperature maps (panel (e)), and grayscale density maps (panel (f)). Panel (a) shows the temporal evolution of jet 10 in $\mathrm{HRI_{EUV}}$ on 2024 April 5. At 21:47:56 UT, no jet-like structure is visible. By 21:50:52 UT, we start to see the appearance of a jet. At 21:51:56 UT, a JBP (red arrow) forms at the base, with a current sheet (green arrow) visible just above it, together with the bright spire (cyan arrow) and the associated upward-moving dark structure (white arrow). The jet activity in the observations ceases around 22:01:00 UT. For jet 1, observed during the north polar observation on 2021 September 14, we have shown five snapshots in panel (b). At 03:33:52 UT, the region appeared quiet with no noticeable jet activity. By 03:35:52 UT, a JBP (red arrow) had formed at the base with a current sheet above it (green arrow), along with a developing bright spire (cyan arrow). A narrow dark structure (white arrow) appeared on the right side of the spire and became more evident at 03:36:32 UT. By 03:38:12 UT, the dark structure had faded, although the bright spire remained visible. Later, at 03:39:52 UT, other dynamic structures emerged in the vicinity, indicating ongoing activity in the region. This jet has also been studied previously by S. Mandal et al. (2022) using AIA data.

The temporal evolution of jet 7, observed on 2022 March 30, is shown in panel (c). At 04:48:42 UT, no significant jet activity was observed. A few minutes later, at 04:51:45 UT, a JBP (red arrow) had formed at the base with a current sheet (green arrow) above it, together with a faint loop-like structure and a developing jet spire (cyan arrow). By 04:53:48 UT, the spire became clearer and a dark structure (white arrow) appeared on the right side. The dark structure became more distinct by 04:55:00 UT and gradually faded by 04:59:45 UT. Another jet is visible at 04:48:42 UT near coordinates (15, 5); this corresponds to jet 4, which is also included in our analysis. The jets in our observations follow a characteristic temporal evolution: an initially quiescent region, the appearance of a JBP at the base, the formation of a current sheet above it, the development of a bright spire accompanied by dark structures, and, finally, a gradual fading of activity. Overall, the jets closely resemble the evolution of classical jets (K. Shibata et al. 1994; T. Yokoyama & K. Shibata 1995) and exhibit the characteristic inverted "Y" (or "λ") morphology.

Panel (d) shows the synthetic emission in the EUI 174 Å passband from the Bifrost simulation, expressed in units of DN $\mathrm{cm^{-1}\ s^{-1}\ pix^{-1}}$. The jet displays an inverted Y-shaped morphology and a temporal evolution closely resembling our observations. The blue contours at $T = 0.1$ MK trace the transition region and aid the identification of the cool ejection, while the red contours at $T = 2$ MK outline the hot plasma around the JBP, current sheet, and spire. The spire at $T = 2$ MK, however, appears dark. This is mainly due to the 2.5D nature of the simulation and the temperature response of the EUI passband, which is centered at 174 Å and is most sensitive to plasma near ∼1 MK through Fe IX and Fe X emission lines. So, plasma that is either significantly cooler or hotter than this peak contributes little to the 174 Å intensity, and thus appears dark. Therefore, we have shown the corresponding temperature maps in panel (e), which clearly confirm the presence of ∼2 MK spire plasma and the ∼0.1 MK cool ejection even though they appear dark in the synthetic emission. Panel (f) shows the density maps in grayscale, in units of $\mathrm{g\,cm^{-3}}$, overplotted with the same temperature contours. These maps reveal that the bright spire corresponds to low-density, high-temperature coronal plasma, whereas the adjacent dark structures on the opposite side of the JBP are associated with higher-density, lower-temperature chromospheric plasma. This close resemblance between the observed and simulated jet morphology and dynamics suggests that the studied jets are consistent with being driven by magnetic flux emergence and reconnection (T. Yokoyama & K. Shibata 1996; R. L. Jiang et al. 2012; F. Moreno-Insertis & K. Galsgaard 2013; D. Nóbrega-Siverio et al. 2016; L. Yang et al. 2018).

We emphasize that, in this study, the simulation is used primarily to provide a qualitative morphological comparison with the observed jets, rather than to establish a one-to-one correspondence. In this simulation, a relatively larger jet is produced owing to the imposed boundary conditions. Due to the finite extent of the computational domain and the limited duration of the run the jet's evolution is restricted by the upper boundary and the simulated time span. The upper boundary of the domain is located at ∼30 Mm, which allows plasma to leave the simulation domain. As a result, the full lifetime and length of the simulated jet were not captured. Nevertheless, within these constraints, we estimate the kinetic energy using the portion of the jet spire contained within the domain at a temperature of 1.5 MK. The spire length is measured from the reconnection site to the top of the visible spire (∼23 Mm) and a width of ∼1 Mm in the y-direction. Assuming a cylindrical geometry, we find that at the 66.67 minute timestamp, when the jet reaches its maximum extent within this domain, the kinetic energy of its spire is $\sim 8.15 \times 10^{24}$ erg. This value is comparable to the kinetic energy range derived for the jetlets (N. E. Raouafi et al. 2023; A. C. Sterling et al. 2024) and is about two orders of magnitude higher than that of the observed jets reported here. Note that the simulation models a single, slightly larger 2.5D jet, whereas the observed jets cover smaller spatial scales with substantial event-to-event variability. Moreover, projection effects can lead to underestimated velocities and lengths in the observations. These differences in spatial scale, dimensionality, and magnetic configuration limit the extent to which a direct quantitative comparison can be made.

We note, however, that alternative mechanisms, such as minifilament eruptions, cannot be ruled out. The lack of sufficiently high-resolution observations prevents us from unambiguously determining whether the dark material observed in EUV images corresponds to filamentary plasma or not. Moreover, the absence of magnetic field

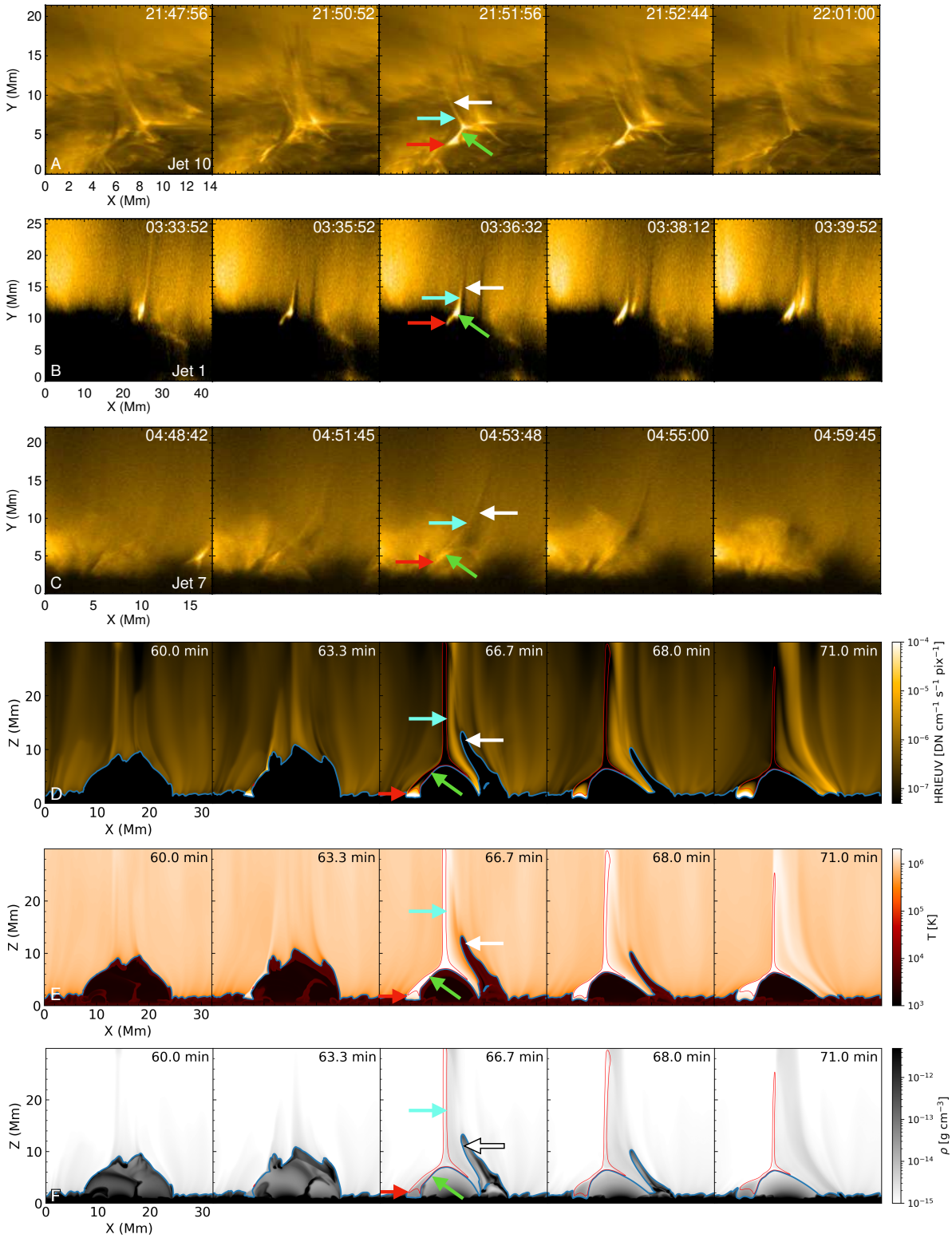

Figure 4. Temporal evolution of jets and comparison with the simulation. Panel (a) shows the temporal evolution of jet 10 observed on 2024 April 5. Panel (b) shows the temporal evolution of jet 1 observed on 2021 September 14 during the north polar observation. Panel (c) shows the temporal evolution of jet 7 observed on 2022 March 30. Panel (d) shows a comparison with a flux-emergence simulation from D. Nóbrega-Siverio et al. (2018), showing synthetic emission in the HRI_{EUV} 174 Å filter. The blue and red contours correspond to plasma at $T = 0.1$ MK and $T = 2$ MK, highlighting the locations of the cool and hot ejections, respectively. The red, green, cyan, and white arrows mark the JBP, current sheet, bright spire, and dark structure, respectively. Panels (e)–(f) show the temporal evolution of the temperature and density maps of the jets, with the same temperature contours from Panel d overlaid. Note that the 2.5D synthetic 174 Å image appears dark in regions where plasma temperatures lie outside the passband's sensitivity, such as the ∼2 MK spire and ∼0.1 MK dark jet; however, the temperature maps clearly reveal them. The animation of panels (d)–(f) is available online. The animation shows the sequence from 50.0 to 71.0 minutes. The real-time duration of the animation is 13 s.

(An animation of this figure is available in the online article.)

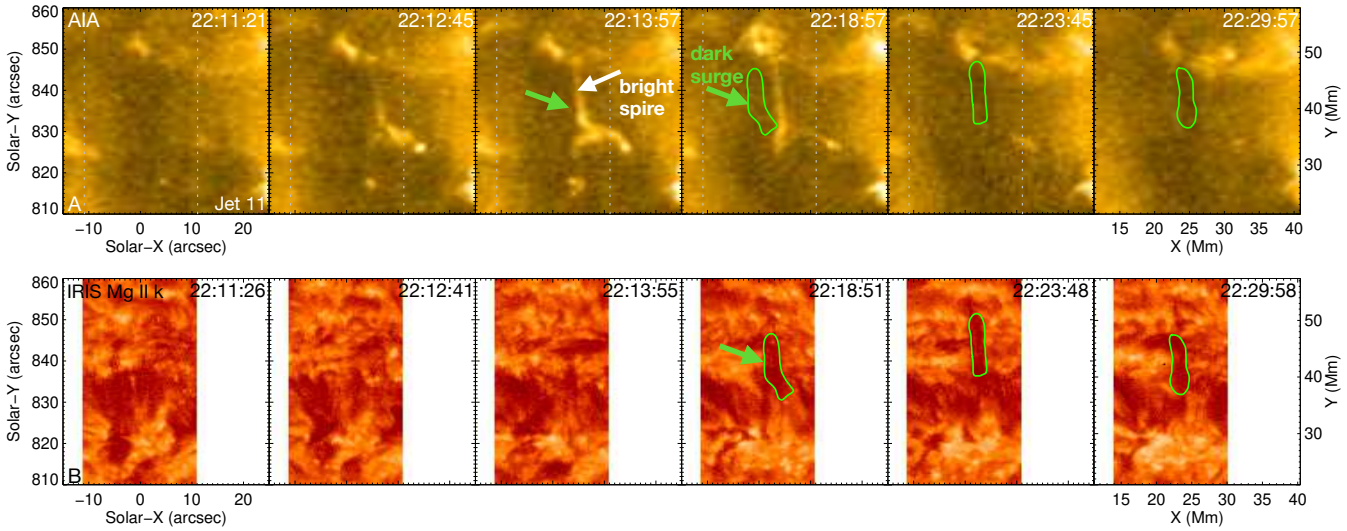

Figure 5. Panel (a): temporal evolution of jet 11 observed in the AIA 171 Å passband on 2019 August 7. The jet base exhibits a distinct inverted "Y" (or "λ") morphology, most clearly visible at the 22:13:57 timestamp. Panel (b): coordinated IRIS observation showing the temporal evolution of raster maps, constructed by extracting the intensity at 2796.2 Å in the Mg II k spectral window. The green contour outlines the dark surge observed in Mg II k 2796.2 Å and is overplotted in the AIA 171 Å images in panel (a), revealing that the dark surge appears adjacent to the bright jet spire. The white vertical dashed line in the AIA panels marks the FOV of the IRIS raster maps. An animation of this figure is available online. The animation starts at 2019 August 7 at 22:00:21 UT and ends the same day at 22:59:57 UT. The real-time duration of the animation is 5 s.

(An animation of this figure is available in the online article.)

measurements precludes us from establishing whether these jets are driven by flux cancellation or flux emergence. Some of the jets we visually inspected could be related to minifilament eruptions, as reported in earlier studies using HRI_{EUV} observations (S. Mandal et al. 2022; D. M. Long et al. 2023). However, in the absence of radiative-MHD simulations for the minifilament scenario, our comparison is limited to the available flux-emergence simulations, and the one-to-one correspondence between our observations and these simulations suggests that flux emergence might be responsible for driving the jets in our study. While future minifilament eruption simulations will allow direct comparisons and will provide valuable complementary insights, coordinated high-resolution limb magnetograms and chromospheric imaging (Hα, Ca II, Mg II), combined with multiwavelength EUV observations and Doppler diagnostics (e.g., H. Chen et al. 2020), will also be essential to gain critical insight into the minifilament scenario.

2.6. Chromospheric Nature of Dark Structures

These dark structures share key morphological and dynamical properties with previously reported chromospheric surges (J. R. Roy 1973; R. C. Canfield et al. 1996; Y. C. Jiang et al. 2007). With the unprecedented spatial resolution and high cadence of HRI_{EUV}, we analyzed 10 tiny coronal jets observed at the solar poles in EUV. To complement our analysis we also utilize the coordinated IRIS and AIA observations (dataset D5), which provide diagnostics in chromospheric lines such as Mg II, allowing us to study the dark structure seen in our tiny coronal jets in greater detail alongside the EUV data.

Figure 5 shows the evolution of jet 11 in these coordinated AIA and IRIS observations. Panel (a) shows the evolution of jet 11 in AIA 171 Å. To analyze its chromospheric component, we used the Mg II k 2796 Å spectral window from IRIS, which primarily samples chromospheric plasma at temperatures of $\log T = 3.7$–4.2 K. Afterward, we created intensity raster maps by extracting the intensity at 2796.2 Å, which corresponds to the position of the k2v emission peak, from each slit position as IRIS scanned across the region. Each full map was made at a cadence of 74 s. In the raster maps, a dark collimated structure, identified as a "chromospheric surge" (highlighted by a green contour), is observed. When the same contour is overplotted on the AIA images, the surge lies immediately adjacent to the bright jet spire on the side opposite the JBP (marked with a white arrow). The jet exhibits an inverted "Y" (or "λ") morphology with a narrow spire emerging from a broader base and the surge detected in IRIS aligns closely with the bright spire in AIA. This configuration is consistent with the standard flux-emergence scenario, as reproduced in the numerical simulations presented in this paper and also in previous studies (T. Yokoyama & K. Shibata 1995, 1996; R. L. Jiang et al. 2012; F. Moreno-Insertis & K. Galsgaard 2013; L. Yang et al. 2018). This one-to-one spatial correspondence suggests that the dark structure in our EUV observations might be a chromospheric surge associated with a coronal jet.

The identification of the jet as a surge is supported by its morphology and the gradual, collimated rise of cool and dark plasma gradually appearing and disappearing at the same location, which are characteristic features described in earlier studies of surges (J. R. Roy 1973; B. Schmieder et al. 1984; Y. C. Jiang et al. 2007; W. Uddin et al. 2012). Since the jets in our study are located at the limb, direct and reliable measurements of the underlying photospheric magnetic field are unfortunately not available. In the future, we hope that high-resolution magnetogram observations will enable a more detailed study of these jets and provide crucial insights into their magnetic configuration.

3. Summary

Picoflare jets are the smallest reconnection-driven jets observed in the solar atmosphere and have been proposed as potential contributors to coronal heating and solar wind acceleration, yet their physical origin remains elusive. In this study we examined tiny coronal jets observed off-limb in the Sun's polar regions using high-resolution observations from the HRI_{EUV} on board Solar Orbiter. These jets, which we identify as picoflare-scale events, often display the simultaneous presence of a bright spire and a narrow, collimated dark structure. Our analysis shows that their spatial (length: 7.85–29.74 Mm; width: 0.35–1.75 Mm) and temporal scales (3.4–11.5 minutes) are comparable to those of jetlets, while their kinetic energies (7.30×10^{21}–9.98×10^{22} erg) fall within the picoflare regime. By combining coordinated observations from IRIS and AIA on board SDO with insights from Bifrost radiative-MHD simulations, we find a clear one-to-one morphological correspondence between the dark counterparts and cool chromospheric surges accompanying the bright spire. Our findings suggest that these small-scale, jetlet-like picoflare jets are driven by magnetic reconnection following magnetic flux emergence, resulting in coupled bright and dark plasma ejections. While coupled bright and dark plasma ejections are well documented in larger coronal jets, our results show that they also occur at the picoflare-jet scale, suggesting a unifying reconnection-driven mechanism across jet regimes. These results underscore the importance of high-resolution observations and models in resolving the fundamental components of solar activity and provide new constraints on the role of small-scale jets in coronal heating and solar wind acceleration.

Acknowledgments

Solar Orbiter is a space mission with international collaboration between ESA and NASA, operated by ESA. The EUI instrument was built by CSL, IAS, MPS, MSSL/UCL, PMOD/WRC, ROB, LCF/IO with funding from the Belgian Federal Science Policy Office (BELSPO/PRODEX PEA 4000134088), the Centre National d'Etudes Spatiales (CNES), the UK Space Agency (UKSA), the Bundesministerium für Wirtschaft und Energie (BMWi) through the Deutsches Zentrum für Luft- und Raumfahrt (DLR), and the Swiss Space Office (SSO). IRIS is a NASA small explorer mission developed and operated by LMSAL with mission operations executed at NASA Ames Research Center and major contributions to downlink communications funded by ESA and the Norwegian Space Centre. D.N.S gratefully acknowledges the support by the European Research Council through the Synergy Grant number 810218 ("The Whole Sun," ERC-2018-SyG) and by the Research Council of Norway (RCN) through its Centres of Excellence scheme, project number 262622. J.J. acknowledges funding support from the SERB-CRG grant (CRG/2023/007464) provided by the Anusandhan National Research Foundation, India.

Facilities: SolO (EUI), IRIS, SDO (AIA).

*S*oftware: IDL (B. Stern 2000).

ORCID iDs

Annu Bura https://orcid.org/0009-0000-5018-9735
Daniel Nóbrega-Siverio https://orcid.org/0000-0002-7788-6482
Tanmoy Samanta https://orcid.org/0000-0002-9667-6392
Jayant Joshi https://orcid.org/0000-0003-0585-7030

References

Adams, M., Sterling, A. C., Moore, R. L., & Gary, G. A. 2014, ApJ, 783, 11
Anzer, U., & Heinzel, P. 2005, ApJ, 622, 714
Bai, X., Socas-Navarro, H., Nóbrega-Siverio, D., et al. 2019, ApJ, 870, 90
Berghmans, D., Auchère, F., Long, D. M., et al. 2021, A&A, 656, L4
Bhatnagar, A., Prasad, A., Nóbrega-Siverio, D., Rouppe van der Voort, L., & Joshi, J. 2025, A&A, 698, A174
Bose, S., Joshi, J., Henriques, V. M. J., & Rouppe van der Voort, L. 2021, A&A, 647, A147
Bose, S., Joshi, J., Testa, P., & De Pontieu, B. 2025, ApJL, 983, L7
Bose, S., Nóbrega-Siverio, D., De Pontieu, B., & Rouppe van der Voort, L. 2023, ApJ, 944, 171
Bura, A., Samanta, T., Prasad, A., et al. 2025a, ApJL, 985, L47
Bura, A., Shrivastav, A. K., Patel, R., et al. 2025b, ApJL, 988, L65
Canfield, R. C., Reardon, K. P., Leka, K. D., et al. 1996, ApJ, 464, 1016
Chae, J., Qiu, J., Wang, H., & Goode, P. R. 1999, ApJL, 513, L75
Chen, H., Hong, J., Yang, B., Xu, Z., & Yang, J. 2020, ApJ, 902, 8
Chen, H., Jiang, Y., & Ma, S. 2009, SoPh, 255, 79
Chitta, L. P., Peter, H., Parenti, S., et al. 2022, A&A, 667, A166
Chitta, L. P., Zhukov, A. N., Berghmans, D., et al. 2023, Sci, 381, 867
Chitta, L. P., Huang, Z., D'Amicis, R., et al. 2025, A&A, 694, A71
de Pontieu, B., McIntosh, S., Hansteen, V. H., et al. 2007, PASJ, 59, S655
De Pontieu, B., Title, A. M., Lemen, J. R., et al. 2014, SoPh, 289, 2733
Feldman, U., Doschek, G. A., Mariska, J. T., Bhatia, A. K., & Mason, H. E. 1978, ApJ, 226, 674
Gao, Y., Tian, H., Berghmans, D., et al. 2025, ApJL, 985, L12
Gorman, J., Chitta, L. P., & Peter, H. 2022, A&A, 660, A116
Gudiksen, B. V., Carlsson, M., Hansteen, V. H., et al. 2011, A&A, 531, A154
He, J. S., Marsch, E., Curdt, W., et al. 2010, A&A, 519, A49
Hong, J., Jiang, Y., Zheng, R., et al. 2011, ApJL, 738, L20
Innes, D. E., Inhester, B., Axford, W. I., & Wilhelm, K. 1997, Natur, 386, 811
Jiang, R. L., Fang, C., & Chen, P. F. 2012, ApJ, 751, 152
Jiang, Y. C., Chen, H. D., Li, K. J., Shen, Y. D., & Yang, L. H. 2007, A&A, 469, 331
Joshi, R., Chandra, R., Schmieder, B., et al. 2020, A&A, 639, A22
Joshi, R., Rouppe van der Voort, L., Schmieder, B., et al. 2024, A&A, 691, A198
Kahil, F., Hirzberger, J., Solanki, S. K., et al. 2022, A&A, 660, A143
Kraaikamp, E., Gissot, S., Stegen, K., et al. 2023, SolO/EUI Data Release 6.0 (2023-01), Royal Observatory of Belgium (ROB), doi: 10.24414/z818-4163
Kumar, P., Karpen, J. T., Antiochos, S. K., et al. 2019, ApJ, 873, 93
Kuridze, D., Mathioudakis, M., Jess, D. B., et al. 2011, A&A, 533, A76
Lemen, J. R., Title, A. M., Akin, D. J., et al. 2012, SoPh, 275, 17
Li, X., Keppens, R., & Zhou, Y. 2023, ApJL, 947, L17
Long, D. M., Chitta, L. P., Baker, D., et al. 2023, ApJ, 944, 19
MacTaggart, D., Guglielmino, S. L., Haynes, A. L., Simitev, R., & Zuccarello, F. 2015, A&A, 576, A4
Mandal, S., Chitta, L. P., Peter, H., et al. 2022, A&A, 664, A28
Moore, R. L., Cirtain, J. W., Sterling, A. C., & Falconer, D. A. 2010, ApJ, 720, 757
Moore, R. L., Sterling, A. C., Falconer, D. A., & Robe, D. 2013, ApJ, 769, 134
Moreno-Insertis, F., & Galsgaard, K. 2013, ApJ, 771, 20
Moreno-Insertis, F., Galsgaard, K., & Ugarte-Urra, I. 2008, ApJL, 673, L211
Mulay, S. M., Del Zanna, G., & Mason, H. 2017, A&A, 606, A4
Müller, D., St. Cyr, O. C., Zouganelis, I., et al. 2020, A&A, 642, A1
Narang, N., Arbacher, R. T., Tian, H., et al. 2016, SoPh, 291, 1129
Narang, N., Verbeeck, C., Mierla, M., et al. 2025, A&A, 699, A138
Nisticò, G., Bothmer, V., Patsourakos, S., & Zimbardo, G. 2009, SoPh, 259, 87
Nóbrega-Siverio, D., Cabello, I., Bose, S., et al. 2024, A&A, 686, A218
Nóbrega-Siverio, D., Joshi, R., Sola-Viladesau, E., Berghmans, D., & Lim, D. 2025, A&A, 702, A188
Nóbrega-Siverio, D., Martínez-Sykora, J., Moreno-Insertis, F., & Rouppe van der Voort, L. 2017, ApJ, 850, 153
Nóbrega-Siverio, D., Moreno-Insertis, F., & Martínez-Sykora, J. 2016, ApJ, 822, 18
Nóbrega-Siverio, D., Moreno-Insertis, F., & Martínez-Sykora, J. 2018, ApJ, 858, 8
Panesar, N. K., Hansteen, V. H., Tiwari, S. K., et al. 2023, ApJ, 943, 24
Panesar, N. K., Tiwari, S. K., Berghmans, D., et al. 2021, ApJL, 921, L20
Panesar, N. K., Sterling, A. C., Moore, R. L., et al. 2019, ApJL, 887, L8

Pereira, T. M. D., De Pontieu, B., & Carlsson, M. 2012, ApJ, 759, 18
Pereira, T. M. D., De Pontieu, B., Carlsson, M., et al. 2014, ApJL, 792, L15
Pesnell, W. D., Thompson, B. J., & Chamberlin, P. C. 2012, SoPh, 275, 3
Raouafi, N. E., Patsourakos, S., Pariat, E., et al. 2016, SSRv, 201, 1
Raouafi, N. E., Stenborg, G., Seaton, D. B., et al. 2023, ApJ, 945, 28
Rochus, P., Auchère, F., Berghmans, D., et al. 2020, A&A, 642, A8
Rouppe van der Voort, L., De Pontieu, B., Scharmer, G. B., et al. 2017, ApJL, 851, L6
Roy, J. R. 1973, SoPh, 32, 139
Samanta, T., Pant, V., & Banerjee, D. 2015, ApJL, 815, L16
Samanta, T., Tian, H., Yurchyshyn, V., et al. 2019, Sci, 366, 890
Schmieder, B. 2022, FrASS, 9, 820183
Schmieder, B., Mein, P., Martres, M. J., & Tandberg-Hanssen, E. 1984, SoPh, 94, 133
Shen, Y. 2021, RSPSA, 477, 217
Shen, Y., Liu, Y., Su, J., & Deng, Y. 2012, ApJ, 745, 164
Shen, Y., Liu, Y. D., Su, J., Qu, Z., & Tian, Z. 2017, ApJ, 851, 67
Shi, F., Li, D., Ning, Z., et al. 2024, A&A, 686, A279
Shibata, K., Nitta, N., Strong, K. T., et al. 1994, ApJL, 431, L51
Shibata, K., Ishido, Y., Acton, L. W., et al. 1992, PASJ, 44, L173
Shimojo, M., Hashimoto, S., Shibata, K., et al. 1996, PASJ, 48, 123
Sterling, A. C., & Moore, R. L. 2016, ApJL, 828, L9
Sterling, A. C., & Moore, R. L. 2020, ApJL, 896, L18
Sterling, A. C., Moore, R. L., Falconer, D. A., & Adams, M. 2015, Natur, 523, 437
Sterling, A. C., Moore, R. L., Falconer, D. A., et al. 2016, ApJ, 821, 100
Sterling, A. C., Moore, R. L., Panesar, N. K., et al. 2020, ApJ, 889, 187
Sterling, A. C., Panesar, N. K., & Moore, R. L. 2024, ApJ, 963, 4
Sterling, A. C., Schwanitz, C., Harra, L. K., et al. 2022, ApJ, 940, 85
Stern, B. 2000, in Proc. Space 2000, ed. S. Johnson, K. M. Chua, R. G. Galloway et al., 1011
Tian, H., DeLuca, E. E., Cranmer, S. R., et al. 2014, Sci, 346, 1255711
Tian, H., Yurchyshyn, V., Peter, H., et al. 2018, ApJ, 854, 92
Uddin, W., Schmieder, B., Chandra, R., et al. 2012, ApJ, 752, 70
Vargas Domínguez, S., Kosovichev, A., & Yurchyshyn, V. 2014, ApJ, 794, 140
Verma, M., Denker, C., Diercke, A., et al. 2020, A&A, 639, A19
Wyper, P. F., Antiochos, S. K., & DeVore, C. R. 2017, Natur, 544, 452
Yang, H., Chae, J., Lim, E.-K., et al. 2013, SoPh, 288, 39
Yang, L., Peter, H., He, J., et al. 2018, ApJ, 852, 16
Yokoyama, T., & Shibata, K. 1995, Natur, 375, 42
Yokoyama, T., & Shibata, K. 1996, PASJ, 48, 353